A Limb Compliant Sensing Strategy for Robot Collision Reaction

Colin Miyata, Kyle Chisholm, Jennifer Baba, and Mojtaba Ahmadi, *Member, IEEE*

***Abstract*—This paper introduces a compliant limb sensor (CLS) concept for collision detection during robot–human contact. The CLS consists of an external rigid shell compliantly connected to the robot link with collision inferred from measured shell displacements. Measuring displacement of a rigid shell allows customizable compliance and high sampling rates due to the small number of required sensors. The proposed sensor is prototyped for the planar case using LED/light-to-voltage (LTV) sensors for shell pose measurement and foam as the compliant link between the shell and base. A physically motivated model for the output of LED/LTV sensor pairs is formulated for the estimation of the shell pose. Voltage measurements of redundant LTVs and a calibrated shell model are used with an iterative optimization routine to estimate the shell pose at high frequencies. Sensor performance is tested using five trajectories: rest, compression, shear, rotation, and arbitrary motion. Experiments confirmed that the CLS can sense the presence, direction, and intensity of impact. The potential application of the proposed sensor to safety in physical human–robot interaction is discussed. The novel sensing methodology also enables a new method of 3-D human–computer interaction due to the ability to modify the compliance and operating range of the CLS.**

I. Introduction

With advancing robot technologies, new applications involving physical human–robot interaction (pHRI) are becoming possible. Due to the shared workspace of the robot and user, unexpected robot–human collisions cannot be avoided [1] and are capable of harming the user [2]–[4]. Notably, unexpected collisions in the emerging fields of lower-limb rehabilitation robotics [5] and human robot comanufacturing [6] pose significant safety concerns due to the strength of the devices. Robots must ensure safety during unexpected collisions.

To prevent injury during unexpected collisions, robots must be capable of rapidly detecting collision while offering suitable mechanical compliance to mitigate injury. Collision detection allows control strategies to avoid the point of collision while mechanical compliance delays and minimizes peak impact forces [7]. Model-based collision detection using joint torque sensors [8] and structural compliance in the form of compliant links [9] and joints [10]–[12] have been proposed. Unfortunately, in high-torque applications, the relative size of collision forces compared to actuator torques can hide the collision in modeling error [1], while structural compliance limits the control bandwidth of the robot [12], [13]. An alternative strategy aims at estimating the external disturbance by observing the variation of motor torque using dithering [14], [15]. This method relies on estimating dry friction and is effective at almost zero speeds when dry friction is unknown. However, for dynamic maneuvers, a good knowledge of robot or actuator dynamics would still be needed. Joint torque sensor additionally does not detect collisions affecting the null space of the robot motion (null space of the robot Jacobian). Ideally, sensing for any collision in any direction, rotational or translational and for every linkage, should be observable.

Tactile sensing has the potential to offer collision detection and mechanical compliance while maintaining a rigid and powerful robot structure. Sensors composed of compliant materials can directly measure forces and deformations along the robot surface to determine if collision has occurred and the severity of the impact. As the tactile sensing is added onto the surface of the robot, the sensors do not significantly affect the mechanical performance of the robot. In addition, tactile sensors can be used to retrofit the existing manipulators for possible pHRI applications.

To be used in robot safety, compliant tactile sensor systems must meet stringent requirements including [16], [17]:

1) low response time;
2) the ability to cover a variety of surfaces;
3) the capacity to absorb impact energy without sensor damage.

A significant effort in the literature has gone to the development of whole body tactile sensing with these ideal characteristics. Attempted tactile sensors span a range of transduction methods including resistive [18], capacitive [16]–[19], and optical [20] measurements and range from simple force sensitive bumpers [21] and arrays of fabric switches [22] to complex pressure sensor arrays employing distributed processing [23].

Over the past decade, the shifting of focus toward safety in pHRI has lead to the development of numerous safety-oriented tactile sensors. In an effort to overcome the sampling and wiring issues of tactile sensor arrays, Battaglia *et al.* [24] developed a multilayer sensor consisting of an underlying force sensor bumper covered by a matrix of push buttons to detect contact and compliant foam. While offering compliance and measuring applied wrenches and contact area, the prototype did not develop the force sensor bumper and the push button matrix suffered a lack of sensitivity due to the compliant coating. Lamy *et al.* [7] developed a robotic skin for safety with industrial robots

Manuscript received November 3, 2014; accepted September 22, 2015. Date of publication October 30, 2015; date of current version February 24, 2016. Recommended by Technical Editor S. Nahavandi. This work was supported by Natural Sciences and Engineering Council Canada grants.

The authors are with the Mechanical and Aerospace Engineering Department, Carleton University, Ottawa, ON K1S 5B6, Canada. (e-mail: colinmiyata@cmail.carleton.ca; kylechisholm@cmail.carleton.ca; jennifer_baba@carleton.ca; mahmadi@mae.carleton.ca).

Digital Object Identifier 10.1109/TMECH.2015.2496553

that employed an array of force sensitive resistors covered by a compliant foam. While achieving high sampling rates, the sensor displayed a transient response time of 2 ms and hysteresis in the sensor output. A foam sensor array with integrated LED and light sensors was developed to detect 3-D deformation of soft skin for humanoid robotics [25], but the data processing of the prototype is not effectively characterized and does not demonstrate reliable sensor information. More recently, an initial prototype of the DLR artificial skin [26], [27] has been developed exploiting variable contact electrodes to measure forces using resistance. The prototype focuses on practical application to pHRI and has been demonstrated to be scalable, durable, and sensitive; however, the current setup still faces challenges in data acquisition and requires development of the transduction method. Overall, no current tactile sensor is suitable to ensure safety during pHRI.

Force transduction or touch sensing with a compliant mechanism have been investigated for safe pHRI collision detection. Another approach proposed in this paper is to employ a lightweight rigid shell connected to the robot with a compliant interface material to provide a deformable point of contact in case of collision. A minimalistic customizable tactile sensor dubbed the compliant limb sensor (CLS) is proposed as a practical whole body tactile sensing for safety in pHRI. If the CLS outer shell pose relative to each robot linkage is measured reliably and accurately, at high frequencies and low latency, it could effectively detect and characterize any collision with the robot and provide some compliance to avoid injury to the user. High compliance of the CLS allows for higher displacements, which can enhance the user precision in a 3-D input device and enable safer interactive robotic systems. Applied forces and moments may be inferred from the displacements, and either the measured deformations or the calculated forces and moments can be used as feedback to respond to collision.

By measuring the displacements of a rigid shell, the solution reduces the number of required sensors and decouples the transduction from the mechanical properties of the shell. Decreasing the number of sensors, high sampling rates and improved response times can be achieved while avoiding excessive wiring. As the CLS consists of an external shell with an adjustable connection to the robot link, the sensor can cover an arbitrary robot link within the constraints imposed by the chosen displacement sensors. By decoupling the transduction from the materials used, the proposed sensor allows for customizable mechanical properties, including viscoelasticity and nonlinear stiffness. It should be noted that while the material is arbitrary, the use of highly viscoelastic materials would result in difficulties in modeling the sensor shell to infer applied forces and moments. However, displacement can be used directly for feedback and inexact force measurements resulting from the use of such materials would still indicate the presence and general severity of a collision.

For measuring the displacements, many commercial sensors exist, but do not meet the needs of collision in pHRI. Vision-based motion capture systems such as the Optotrak, PS move, Wiimote, Kinect, etc., do not meet the need for a high-frequency (≈ 2000 Hz) compact integrated sensor. Vision systems suffer from the line-of-sight issues, low-frequency operation (20–100 Hz), and require external hardware that is expensive and difficult to integrate with articulated multi-DoF robotic systems. The 3-D mouse and desktop input devices, such as the Globefish [28] or 3-D Connexion's SpaceMouse [29], also employ pose sensing capabilities. The trackball of the Globefish decouples linear and rotational DoFs and its large base is not suitable for a collision event. The SpaceMouse detects small displacements and estimates 6-DoF pose using optical techniques [29]. The SpaceMouse contains structural and electromechanical components with specific arrangements that cannot easily be scaled to larger shells that would be intended for pHRI applications. In the absence of a compact -frequency compliant 6-DoF sensor with a large range of motion, a novel alternative is proposed for the CLS in this paper. While the proposed solution involves more computationally complex algorithms, it is shown that it can run at high rates, it incorporates simple inexpensive components, and is scalable and capable of accommodating larger range of motion. In light of the applications of the previously discussed sensing technologies, the new CLS sensing strategy may also be applicable as a novel 6-DoF position-sensing input device for interaction with 3-D environments including gaming, CAD software, virtual reality environments, and teleoperation of robots [30], [31].

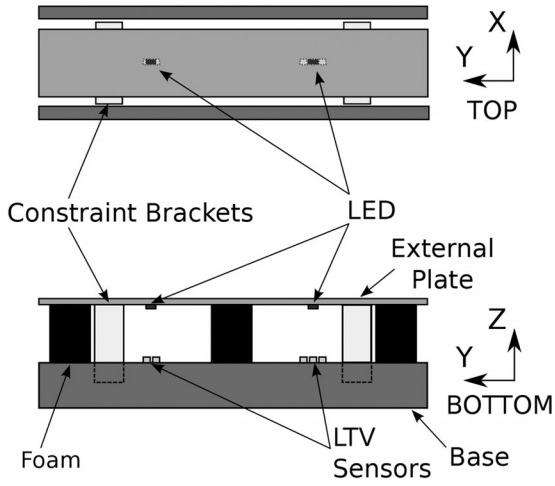

Fig. 1. Overall sensor configuration for the compliant shell.

II. Proposed Solution

This paper seeks to develop a generalized 6-DoF model and the proof of concept planar CLS. A schematic of the proposed sensor is shown in Fig. 1 and Fig. 2 demonstrates the role of the CLS to deform during and sense a robot–human collision. The proof of concept sensor consists of a sandwich structure with three pillars of foam separating the base from the external plate. LEDs combined with the light-to-voltage (LTV) sensors were chosen to measure distance. Optical sensors were chosen for their rapid response time, limited restriction on the motion of the external plate, and low cost.

The rest of this paper presents the development of the proof of concept CLS. Section III presents the design of the current prototype, while the calibration of the sensor shell model is described in Section IV. Experimental validation of sensor

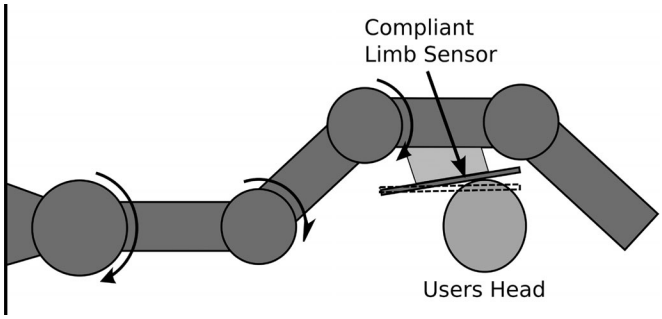

Fig. 2. Proposed use of the CLS during robot–human collisions. A single CLS is shown for clarity. In actual implementation, the CLS shell will cover the entire link.

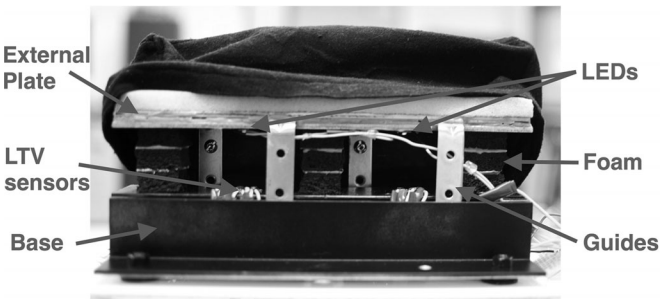

Fig. 3. Proof of concept sensor with labels.

performance is presented in Section V, and Section VI discusses the applicability of CLS to robot safety.

III. Sensor Design

A. Sensor Configuration

The CLS prototype is shown in Fig. 3. In between the foam columns, LEDs were adhered to the external plate and groups of two or three LTV sensors were adhered to the base. All LTV sensors and LEDs were placed on a straight line extending lengthwise along the sensor and the entire sensor was covered in black fabric to prevent external light from affecting the LTV sensor measurements. Brackets extending from the external plate constrain the motion of the shell to translations in the yz plane and rotation about the x-axis. The rigid plate will add inertia to the sensor and will offer a stiff contact with the environment, tending to increase the potential harm to the user. To mitigate this affect, light-weight materials were used for the plate and a thin layer of foam was added.

To implement a light-weight elastic member, a triple layer of extra soft natural gum foam was used. Each column is $1.5\,\text{in}$ tall with a cross sectional area of $1.5\,\text{in}^2$. This material is also desirable for the nonlinear relationship between force and deformation which includes minimal applied force to produce significant deformation before increasing in stiffness at larger strains.

B. Displacement Measurement

The displacement and orientation of the sensor is estimated using the outputs of the LTV sensors and a model of the

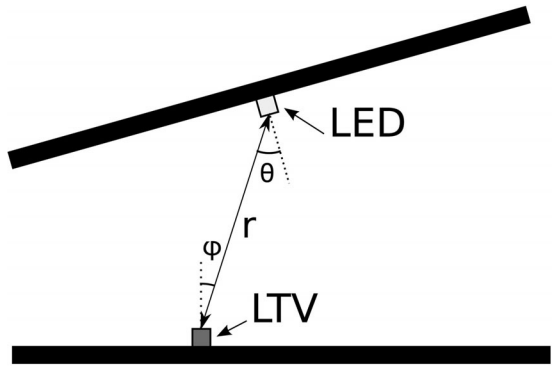

Fig. 4. Schematic of variables effecting LTV output voltage.

LED/LTV sensor pairs. The LEDs and LTV sensors used on the current prototype are Avago Technologies ASMT-QRBD-AEF0E and TAOS TSL252R, respectively. The detected light intensity is affected by the configuration of the LED/LTV sensor pairs through three parameters: the distance between the LTV sensor and LED (r), the angle of incidence of the LED with respect to the LTV sensor (θ), and the angle of incidence of the LTV sensor with respect to the LED (ψ). These parameters are illustrated in Fig. 4.

To model the light intensity detected by the LTV sensor, the light from the LED is assumed to spread as a semisphere from the LED and the amount of irradiance emitted from the LED and detected by the LTV sensor is assumed to be proportional to the observed area of the component from the perspective of the other. The LTV sensor output is proportional to the irradiance of detected light [32] and is inversely proportional to the diffusion of light as it travels from the LED to the LTV sensor. With the assumption of a spherical surface, the LTV sensor voltage would then be inversely proportional to a quadratic relationship of the length r between the LTV and LED. The effect of distance r on the LTV sensor output then takes the form

$$v \propto f_1(r) = \frac{a_1}{r^2 + c_2 r + c_3} \tag{1}$$

where a_1, c_2, and c_3 are parameters to be calibrated for each LTV sensor.

With the assumption that the light emitted and detected by the LED and LTV sensor is proportional to the observed area, the impact of the angle of incidence of each component can be determined using the projection of the component onto the plane perpendicular to the centerline. Noting that the light emitting surface of the LED is flat and the detecting surface of the LTV sensor is a semisphere, the impact of the angles of incidence θ and ϕ take the form

$$v \propto f_2(\theta) = a_2 \cos(c_4 \theta) \tag{2}$$

$$v \propto f_3(\phi) = a_3 (1 + c_5 \cos(c_6 \theta)) \tag{3}$$

where all a_2, a_3, and c_4,...,c_6 are parameters to be calibrated for each LED/LTV sensor.

Let $\eta = [r\ \theta\ \psi]^T$ be a vector of geometric parameters for each LED/LTV sensor pairing. By taking the product of relationships (1)–(3) and normalizing about a set point, the LTV sensor

voltage model for an LTV sensor and LED pair is defined as

$$\begin{aligned} v &= g_v(\mathbf{c},\ \eta) \\ v &= \frac{c_1}{r^2 + c_2 r + c_3} \cos\left(c_4\theta\right)\left(1 + c_5 \cos\left(c_6\psi\right)\right) + c_7 \end{aligned} \quad (4)$$

where $c_1 = (a_1 a_2 a_3)/\nu$, ν is a constant normalizing factor, v is the voltage output for the LTV sensor, and $\mathbf{c} = [c_1\ c_2, \cdots, c_7]^T$ is a vector of model coefficients, including an offset value c_7. It should be noted that the current assumptions and, consequently, the model are not valid when the widths of the LTV sensor and LED are significant relative to the radius or when the angle of incidence is large.

C. Sensor Shell Model

The pose of a coordinate frame is denoted by the vector

$$\mu = \begin{bmatrix} \mathbf{p}^T & q^T \end{bmatrix}^T \quad (5)$$

where position vector $\mathbf{p} \in \mathbb{R}^3$ is the origin of the frame and q is its orientation in unit quaternion representation. This paper uses the quaternion vector space notation $q = \begin{bmatrix} q_w & \mathbf{q}^T \end{bmatrix}^T$, where q_w is the real scalar component and $\mathbf{q} \in \mathbb{R}^3$ is the vector component. Forward and inverse coordinate transformations applied to μ_2 by μ_1 are

$$h(\mu_1, \mu_2) = \begin{Bmatrix} q_1 p_2 q_1^{-1} + p_1 \\ q_1 q_2 \end{Bmatrix} \quad (6)$$

and

$$\bar{h}(\mu_1, \mu_2) = \begin{Bmatrix} q_1^{-1}\left(p_2 - p_1\right) q_1 \\ q_1^{-1} q_2 \end{Bmatrix} \quad (7)$$

respectively, where $p = [0\ \mathbf{p}^T]^T$. For the currently considered yz planar case, the relevant equations for the coordinate transformations are

$$\bar{\mu} = \begin{bmatrix} p_y & p_z & \theta_x \end{bmatrix}^T \quad (8)$$

$$h_{yz}(\bar{\mu}, \mu) = \begin{Bmatrix} (R\theta_x)\,\mathbf{p} + \begin{Bmatrix} 0 \\ p_y \\ p_z \end{Bmatrix} \\ \bar{q}(\theta_x) q \end{Bmatrix} \quad (9)$$

$$\frac{\partial}{\partial \bar{\mu}} h_{yz}(\bar{\mu}, \mu) = \begin{bmatrix} I_{23} & -R(\theta_x)[\mathbf{p}]^{\times} \hat{e}_x \\ \mathbf{0}_{3\times 2} & R(q^{-1})\hat{e}_x \end{bmatrix} \quad (10)$$

where $[\cdot]^{\times}$ denotes a skew-symmetric matrix generated from a vector in 3-space, I_{23} is column 2 and 3 of I_3, $R(\theta_x)$ is a rotation matrix by angle θ_x about the x-axis, $\hat{e}_x$ is a basis unit vector in the x-direction, and

$$\bar{q}(\theta_x) = \exp\left(\frac{1}{2}\begin{bmatrix} 0 & \theta_x & 0 & 0 \end{bmatrix}^T\right). \quad (11)$$

To develop the sensor shell model, coordinate frames were assigned to each LED with the origin at the focal point of the light emitter and the z-axis aligned with the optical axis. The constant pose of the LED relative to the shell is μ_d^s. The

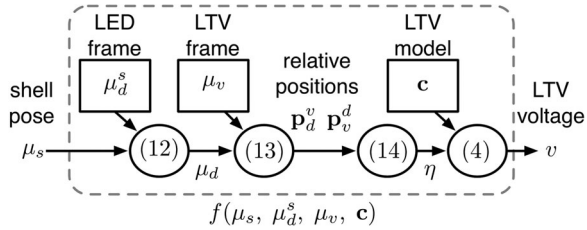

Fig. 5. Model processing from shell pose to voltage output of LTVs. Constants are shown in boxes and operations are shown in circles with referenced equations.

LED pose relative to the base frame is the result of a coordinate transform

$$\mu_d = h(\mu_s, \mu_d^s) \quad (12)$$

where μ_s is the pose of the shell relative to the fixed base.

Similarly, LTV sensor coordinate frames have the origin at the focal point of the light receiver with the z-axis aligned with the sensor optical axis. The constant pose of the LTV sensor relative to the base is μ_v. The relative LTV sensor and LED pair positions are determined from inverse coordinate transforms

$$\begin{aligned} \mu_d^v &= \bar{h}(\mu_v, \mu_d) \\ \mu_v^d &= \bar{h}(\mu_d, \mu_v). \end{aligned} \quad (13)$$

LTV sensor model parameters η were determined from relative positions $\mathbf{p}_d^v$ and $\mathbf{p}_v^d$ as follows:

$$\begin{aligned} \eta &= g_\eta(\mathbf{p}_d^v, \mathbf{p}_v^d) \\ &= \begin{Bmatrix} r \\ \cos^{-1}\left(\frac{\mathbf{p}_d^v \cdot \hat{z}}{r}\right) \\ \cos^{-1}\left(\frac{\mathbf{p}_v^d \cdot \hat{z}}{r}\right) \end{Bmatrix} \end{aligned} \quad (14)$$

where $r = \|\mathbf{p}_d^v\| = \|\mathbf{p}_v^d\|$ and $\hat{z} = [0\ 0\ 1]^T$. The LTV sensor voltage output v can now be determined from shell pose μ_s by applying (12) through (14) and finally (4). The shell model is summarized in Fig. 5 and

$$v = f(\mu_s,\ \mu_d^s,\ \mu_v,\ \mathbf{c}). \quad (15)$$

D. Pose Estimation

The purpose of the shell sensor pose estimation is to find μ_s from measured LTV sensor voltages $\mathbf{v} = [v_1\ v_2,\ \ldots,\ v_n]^T$, where n is the number of LTV sensors. An iterative local optimization approach is applied for solving this nonlinear inverse problem with redundant LTV sensor data given an initial guess $(\mu_s)_0$. The Levenberg–Marquardt (LM) optimization routine was chosen for its robustness, simplicity, and rate of convergence [33]. The optimization problem is to minimize

$$\min S(\mu_s) = \|W\left(\mathbf{f}(\mu_s, \mathbf{x}) - \mathbf{v}\right)\|^2, \mu_s \in \mathbb{R}^7 \quad (16)$$

where $\mathbf{f} = [f_1\ f_2, \ldots, f_n]^T$ is a vector of voltages evaluated from (15), W is a diagonal matrix of scaling factors w_i for $i = 1, \ldots, n$, and $\mathbf{x}$ is vector of independent variables

$$\mathbf{x} = \begin{bmatrix} \mathbf{c}_1^T & \cdots & \mathbf{c}_n^T & (\mu_v)_1^T & \cdots & (\mu_v)_n^T & (\mu_d^s)_1^T & \cdots & (\mu_d^s)_o^T \end{bmatrix}^T \quad (17)$$

where o is the number of LEDs on the shell. The optional scaling factors are chosen based on any variable x using the function $w_i(x) = 1/(1+\zeta(x))$, where

$$\zeta(x) = e^{\left(\frac{x_m - x}{\tau(x_M - x_m)}\right)} + e^{\left(\frac{x - x_M}{\tau(x_M - x_m)}\right)} \tag{18}$$

is an exponential cost function, x_m and x_M are the minimum and maximum limits of a range of x, and τ is a scaling factor that controls the steepness of the boundary curves. This weighting scheme is useful for scaling redundant data points that are out of a specified valid range. The LM routine calculates

$$(\delta\mu_s)_k = -\left(J^T J + \lambda\,\mathrm{diag}(J^T J)\right)^{-1} J^T\left(\mathbf{f}_k - \mathbf{v}\right) \tag{19}$$

at each iteration step k, where J is the Jacobian, $\mathbf{f}_k = \mathbf{f}(\mathbf{x}, (\mu_s)_k)$, and λ is a nonnegative damping factor. The algorithm converges successfully when $(\delta\mu_s)_k < \epsilon \vee \|(\mathbf{f}_k - \mathbf{f}_{k-1}\|^2 < \epsilon$ for tolerance ϵ at iteration k.

The optimization function Jacobian contains partial derivatives of f_i for all LTV sensors with respect to optimization parameter μ_s, as in

$$\frac{\partial f_i}{\partial \mu_s} = \frac{\partial v}{\partial \eta}\cdot\frac{\partial \eta}{\partial \mu_d}\cdot\frac{\partial \mu_d}{\partial \mu_s}. \tag{20}$$

The LTV sensor voltage function (4) partial derivative with respect to η is

$$\frac{\partial v}{\partial \eta} = \begin{bmatrix} c_1\cos(c_4\theta)(c_2+2r)(c_5\cos(c_6\psi)+1)/\gamma^2 \\ -c_1 c_4 \sin(c_4\theta)(c_5\cos(c_6\psi)+1)/\gamma \\ -c_1 c_5 c_6\cos(c_4\theta)\sin(c_6\psi)/\gamma \end{bmatrix}^T \tag{21}$$

where $\gamma = (r^2 + c_2 r + c_3)$. The partial derivative of η geometric parameters (14) with respect to μ_d is

$$\begin{aligned}\frac{\partial \eta}{\partial \mu_d} &= \frac{\partial \eta}{\partial \mathbf{p}_d^v}\cdot\frac{\partial \mathbf{p}_d^v}{\partial \mu_d} + \frac{\partial \eta}{\partial \mathbf{p}_d^v}\cdot\frac{\partial \mathbf{p}_v^d}{\partial \mu_d} \\ &= \begin{bmatrix} \frac{(\mathbf{p}_d^v)^T}{\|\mathbf{p}_d^v\|}R(q_v^{-1}) & 0_{1\times 3} \\ [g_z(\mathbf{p}_d^v)]\,R(q_v^{-1}) & 0_{1\times 3} \\ -\left[g_z(\mathbf{p}_v^d)\right]R(q_d^{-1}) & -\left[g_z(\mathbf{p}_v^d)\right]R(q_d^{-1})[\mathbf{p}_{vd}]^\times \end{bmatrix}\end{aligned} \tag{22}$$

where $\mathbf{p}_{vd} = \mathbf{p}_v - \mathbf{p}_d$ and

$$\begin{aligned}[g_z(\mathbf{p})] &= \frac{\partial}{\partial \mathbf{p}}\cos^{-1}\left(\frac{p_z}{\|\mathbf{p}\|}\right) \\ &= \frac{\left[p_x p_z \quad p_y p_z \quad \left(p_x^2 + p_y^2\right)\right]}{\|\mathbf{p}\|^2\left(p_x^2+p_y^2\right)^{1/2}}.\end{aligned} \tag{23}$$

Finally, the coordinate transform partial derivative of the LED frame μ_d with respect to μ_s is

$$\frac{\partial \mu_d}{\partial \mu_s} = \frac{\partial}{\partial \mu_s}h(\mu_s, \mu_d^s) = \begin{bmatrix} I_3 & -R(q_s)[\mathbf{p}_d^s]^\times \\ \mathbf{0}_3 & R((q_d^s)^{-1}) \end{bmatrix}. \tag{24}$$

For the yz planar case

$$\mu_s = h(\bar{\mu}_s, \mu_{s0}) \tag{25}$$

where μ_{s0} is an initial constant coordinate transform to align the shell frame with the fixed inertial frame so that $\bar{\mu}_s$ is the planar transform of the shell about the fixed frame. The partial derivative in this case becomes

$$\frac{\partial \mu_d}{\partial \bar{\mu}_s} = \frac{\partial h(\mu_d^s, \mu_s)}{\partial \mu_s}\cdot\frac{\partial h(\bar{\mu}_s, \mu_{s0})}{\partial \bar{\mu}_s}. \tag{26}$$

IV. Shell Calibration

A. Initial Calibration

To confirm the validity of the proposed model for the LTV sensors, an initial calibration was performed to quantify the response of the LTV sensor and determine an estimate of the model parameters. Experiments were performed using a ball screw actuator to allow linear motion and a motor to provide angular rotations. In (1)–(3), the effects of each property were independent and so the effect of each was quantified in three separate experiments: 1) the LTV sensor moving linearly with respect to the LED to quantify the effect of r, 2) the LED rotating relative to a fixed LTV sensor to quantify the effect of θ, and 3) the LTV sensor rotating relative to a fixed LED to quantify the effect of ψ. The linear and angular positions were measured using a potentiometer attached to the ball screw and an encoder attached to the motor, respectively. Position and LTV sensor output was collected at a sampling rate of 1 kHz.

The results of the experiments were fit using the curve fitting tool box in MATLAB. Sample fits can be seen in Fig. 6. The resulting curves indicate the assumed forms fit well for angles and distances examined; however, the response does deviate from the assumed forms with shorter radii and larger angles of incidence.

B. Batch Calibration

The batch calibration procedure involves refining the parameters determined in the initial calibration in Section IV-A for a completely assembled shell sensor. Independent pose measurements of μ_s and LTV sensor voltage data $\mathbf{v}$ were collected for m arbitrary poses of the shell frame. Given an initial guess of $\mathbf{x}_0$, an iterative optimization routine similar to the pose estimation algorithm was performed with the objective function

$$\min S(\mathbf{x}) = \|\mathbf{F}(\mathbf{x}, \mathbf{U}_s) - \mathbf{V} + \zeta(\theta)\|^2, x \in \mathbb{R}^{13n+7o} \tag{27}$$

where $\mathbf{V} = [\mathbf{v}_1^T\ \mathbf{v}_2^T \cdots \mathbf{v}_m^T]^T$ is a $(nm \times 1)$ vector of LTV sensor voltages measured for m independent poses of μ_s, $\mathbf{U}_s = [\mu_1^T\ \mu_2^T \cdots \mu_m^T]^T$ is $(7m \times 1)$ vector of independent pose measurements, and $\mathbf{F} = [\mathbf{f}_1^T\ \mathbf{f}_2^T \cdots \mathbf{f}_m^T]^T$ is a $(mn \times 1)$ vector of LTV sensor voltages determined from (15) at all m shell frame poses. The cost function $\zeta(\theta)$ from (18) constrains the LTV z-axes to point toward the LEDs.

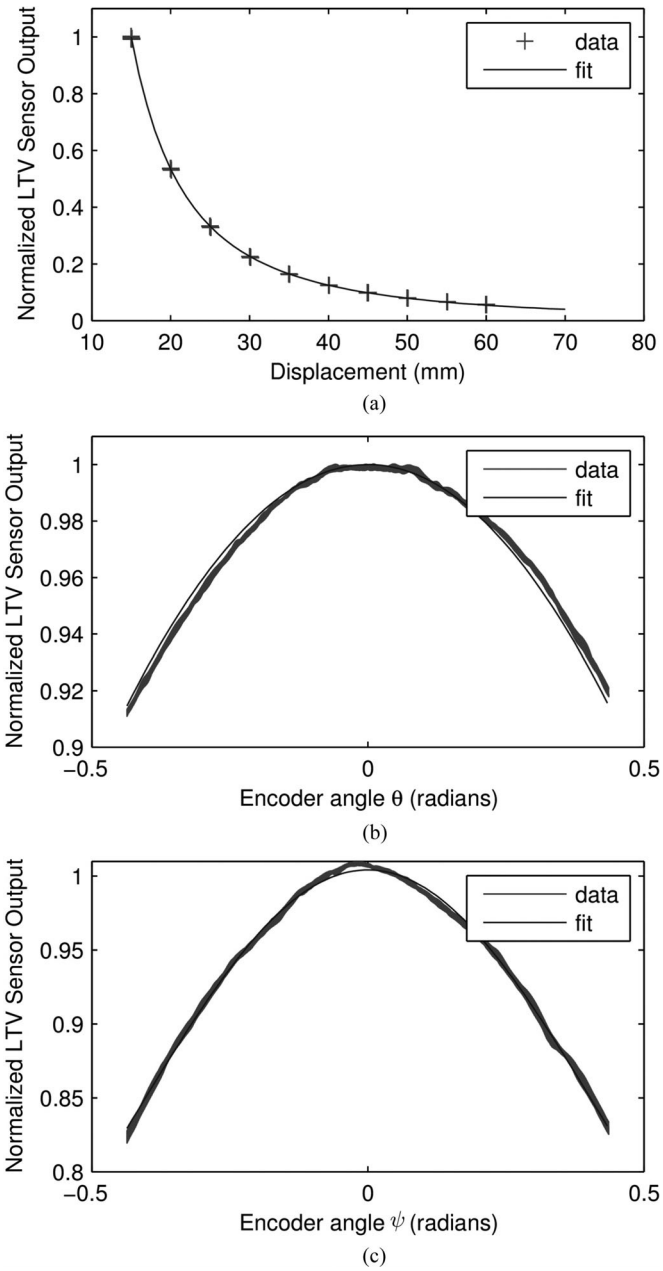

Fig. 6. Sample fits of LTV sensor output with variations in geometric parameters. (a) Measured and fit LTV sensor response to variations in r. (b) Measured and fit LTV sensor response to variations in θ. (c) Measured and fit LTV sensor response to variations in ψ.

The calibration Jacobian J_x is computed by finding the submatrices

$$\frac{\partial f_i}{\partial \mathbf{c}_i} = \frac{\partial v}{\partial \mathbf{c}} \tag{28}$$

$$\frac{\partial f_i}{\partial (\mu_v)_i} = \frac{\partial (v + \zeta(\theta))}{\partial \eta} \cdot \frac{\partial \eta}{\partial \mu_v} \tag{29}$$

$$\frac{\partial f_i}{\partial (\mu_d^s)_j} = \frac{\partial (v + \zeta(\theta))}{\partial \eta} \cdot \frac{\partial \eta}{\partial \mu_d} \cdot \frac{\partial \mu_d}{\partial \mu_d^s} \tag{30}$$

for all LTVs $i = 1, \ldots, n$ and LEDs $j = 1, \ldots, o$ at every measured shell pose $(\mu_s)_p$ where $p = 1, \ldots, m$ so that J_x is a $(nm) \times (12n + o)$ matrix.

and its partial derivative with respect to $\mathbf{c}$ is

$$\frac{\partial v}{\partial \mathbf{c}} = \frac{1}{\gamma} \begin{bmatrix} \cos(c_4\theta)\beta \\ -c_1 r \cos(c_4\theta)\beta/\gamma \\ -c_1 \cos(c_4\theta)\beta/\gamma \\ -c_1\theta \sin(c_4\theta)\beta \\ c_1 \cos(c_6\psi)\cos(c_4\theta) \\ c_1 c_5 \psi \cos(c_4\theta)\sin(c_6\psi) \\ 1 \end{bmatrix}^T \tag{31}$$

where $\beta = c_5 \cos(c_6\psi) + 1$. The partial derivative of η with respect to μ_v is

$$\begin{aligned} \frac{\partial \eta}{\partial \mu_v} &= \frac{\partial \eta}{\partial \mathbf{p}_d^v} \cdot \frac{\partial \mathbf{p}_d^v}{\partial \mu_v} + \frac{\partial \eta}{\partial \mathbf{p}_v^d} \cdot \frac{\partial \mathbf{p}_v^d}{\partial \mu_v} \\ &= \begin{bmatrix} -\frac{(\mathbf{p}_d^v)^T}{\|\mathbf{p}_d^v\|} R(q_v^{-1}) & -\frac{(\mathbf{p}_d^v)^T}{\|\mathbf{p}_d^v\|} R(q_v^{-1})[\mathbf{p}_{dv}]^\times \\ -[g_z(\mathbf{p}_d^v)]\, R(q_v^{-1}) & -[g_z(\mathbf{p}_d^v)]\, R(q_v^{-1})[\mathbf{p}_{dv}]^\times \\ [g_z(\mathbf{p}_v^d)]\, R(q_d^{-1}) & 0_{1\times 3} \end{bmatrix} \end{aligned} \tag{32}$$

where $\mathbf{p}_{dv} = \mathbf{p}_d - \mathbf{p}_v$. The coordinate transform partial derivative of the LED frame μ_d with respect to μ_d^s is

$$\frac{\partial \mu_d}{\partial \mu_d^s} = \frac{\partial}{\partial \mu_d^s} h(\mu_s, \mu_d^s) = \begin{bmatrix} R(q_s) & \mathbf{0}_3 \\ \mathbf{0}_3 & I_3 \end{bmatrix}. \tag{33}$$

The batch calibration was performed using a 37-s calibration trajectory. The τ factor for the cost function for calibration $\zeta(\theta)$ was set to $\tau = 1/40$ and limits set to ± 45 °. Based on the initial guess, data were ignored greater than $\theta = 40$ °, below $r = 20$ mm and voltages greater than $0.8\,V$ for the calibration. The LM routine was performed using the *lsqonlin* function in MATLAB.

V. Experimental Validation

A. Apparatus

The data acquisition system employs a real-time QNX computer with a QPID DAQ from Quanser to gather voltage data from the LTV sensors and an NDI Optotrak Certus 3-D motion capture system to acquire marker data for coordinate transformation measurements. To coordinate the measured shell poses with the LTV sensor voltages, the Optotrak system was externally triggered by the QNX computer. Voltage data was acquired at 2 kHz and rigid body transformations were acquired at a frequency of 80 Hz.

B. Methods

Shell pose and LTV voltages were collected for five 37-s trials with trajectories applied to the shell. The trajectories chosen for the trials include rest, shear, compression, rotation, and general motion (calibration trajectory). The pose estimation used the previous time-step estimate as the initial value for the LM optimization routine. The weighting function $w_i = w(\theta_i)w(r_i)$ was

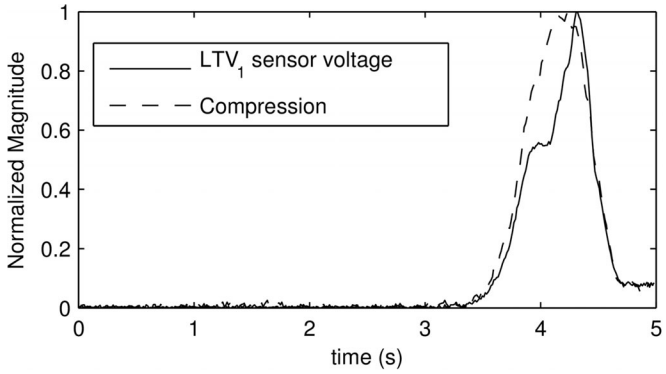

Fig. 7. Normalized LTV_1 voltage and compression for first 5 s of compression trajectory.

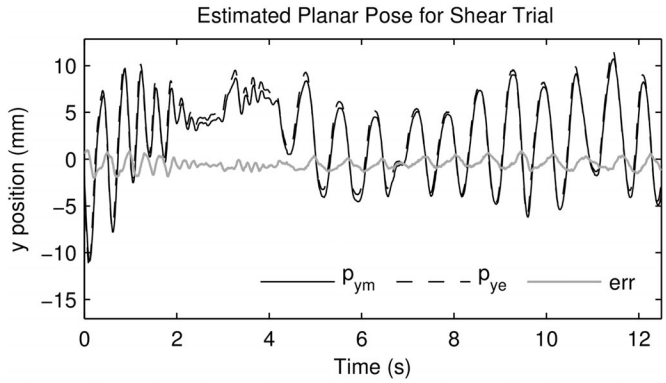

Fig. 8. Estimated planar p_y position from shearing trajectory.

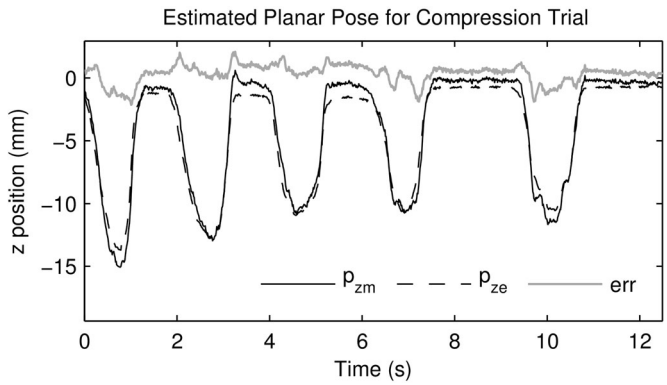

Fig. 9. Estimated planar p_z position from compression trajectory.

set to the bounds $-45° < \theta < 45°$ and $15\,\text{mm} < r < 60\,\text{mm}$ with $\tau = 1/70$. Convergence tolerance was set to $\epsilon = 1e-4$ and a maximum number of 50 iterations per time step. Pose estimation was performed offline using the *lsqonlin* function in MATLAB and reimplemented in C for realtime operation using CMinpack *lmder* routine [34].

C. Results

1) LTV Response to Shell Motion: Fig. 7 shows normalized LTV voltage and compression values over time for the compression trial. LTV sensor voltages respond immediately with shell motion, as would be expected from the sensor response time [32]. During the rest trajectory, LTV sensor outputs

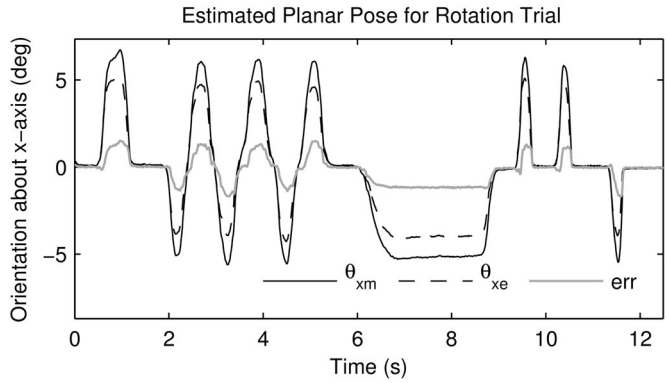

Fig. 10. Estimated planar θ_x position from rotation trajectory.

TABLE I
MEAN AND STANDARD DEVIATION OF ERRORS FOR GIVEN RANGES OF MAXIMUM DEFORMATION OF THE SHELL

		e_y (mm)	e_z (mm)	e_θ (degrees)
$D < 5$ mm	$\bar{x}$	0.9285	0.7905	0.1883
	s	2.8254	2.0494	0.2357
5 mm $< D <$ 10 mm	$\bar{x}$	0.7991	1.9181	0.4850
	s	1.2745	2.4114	0.5825
10 mm $< D <$ 15 mm	$\bar{x}$	0.7514	1.6571	0.3413
	s	0.7838	1.5281	0.4712
$D > 15$ mm	$\bar{x}$	0.5003	2.8460	1.0987
	s	0.5185	1.3311	0.4455

did not vary significantly without shell motion and had an RMS deviation of 0.7 mV from the rest position.

2) Sensor Accuracy: Figs. 8–10 show a sample of the p_y, p_z, and θ_x planar pose results for the shearing, compression, and rotation trajectories, respectively. The mean and standard deviations of error for given ranges of maximum sensor deflection D are given in Table I.

3) Real-Time Performance: Fig. 11 shows a sample of the p_y, p_z, and θ_x planar pose results for the estimated calibration trajectory calculated at 2 kHz. At certain parts of the trajectory, the maximum number of iterations was reached; however, the trajectory did not diverge when run on data sampled at 2 kHz and the average number of iterations at each time step is 7.02.

VI. Discussion

Based on the rapid response of the LTV sensor output to shell motion and the low noise in the signal, change in LTV sensor voltage can be used as a reliable and rapid measure to detect motion from rest. Using LTV sensor output, five sensors would need to be sampled per link at every time step and the process to detect changes to pose would only require a comparison to previous values. Only after motion is detected would pose estimation need to occur, and only on the link where motion was sensed.

While the pose estimation displayed errors of the order of 2 mm, the algorithm did characterize the general motion of the shell, as seen in Figs. 8–10. Errors in the pose estimation can be attributed to errors in the LTV sensor model, and out of

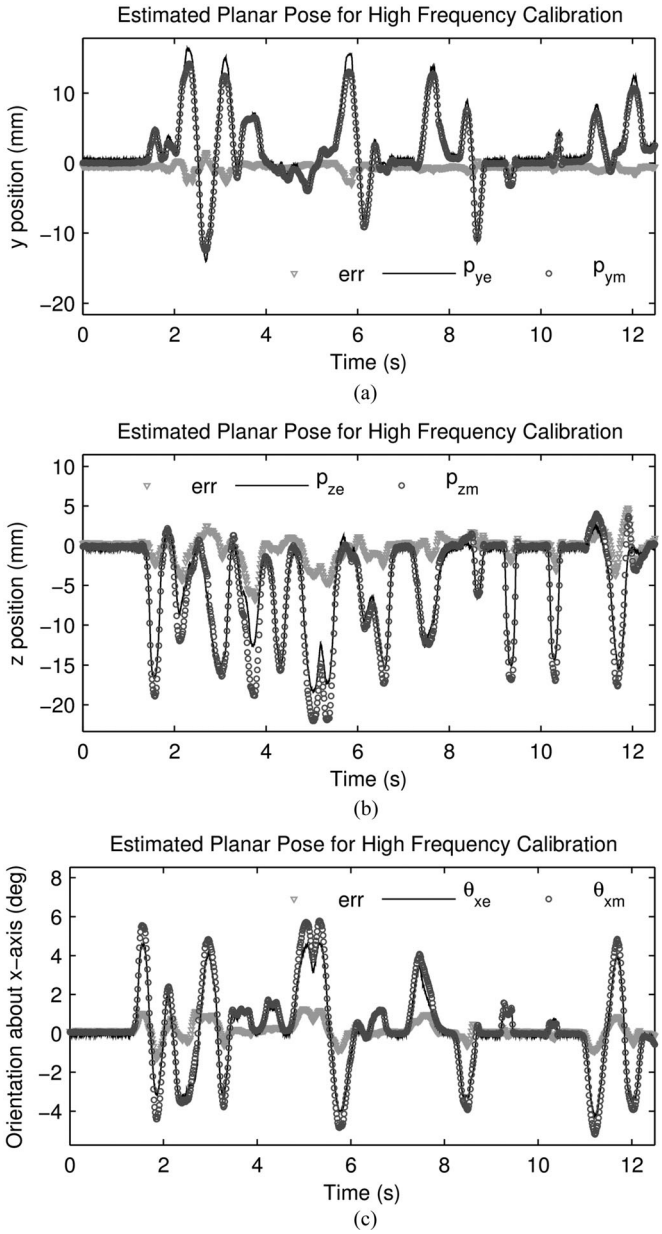

Fig. 11. Estimated calibration trajectory at 2 kHz. (a) Estimated planar p_y position from calibration trajectory at 2 kHz. (b) Estimated planar p_z position from calibration trajectory at 2 kHz. (c) Estimated planar θ_x position from calibration trajectory at 2 kHz.

plane motion unaccounted for in the shell model. Out of plane motion is a possibly significant source of error with motion up to 2.515 mm and 7.34°. The limitation of out of plane motion without significant increase in the shell weight is a further area of development. In addition, the pose estimation was shown suitable for real-time implementation by following the trajectory at 2 kHz with a maximum ten iterations per time step and average optimization computation time of approximately 0.125 ms on a 2.5 GHz Core i5 processor.

In the context of robot safety, the minimal response time, real-time capability, and the customizable mechanical compliance allows the CLS to be an attractive alternative to other currently developed sensors. During an unexpected collision, the CLS would be able to rapidly inform the controller of the impact while minimizing impact forces above the control bandwidth of the robot using the chosen mechanical compliance. As the CLS only requires a small number of analog inputs, the CLS is simple to integrate onto existing robots. It is also important to note that during robot–human collisions, many reaction strategies such as braking and yielding to contact do not require exact information about the collision; rather, only a general measure of intensity and direction are required. The current pose estimation is capable of providing the required details to implement these simple reaction strategies.

As input into a collision reaction strategy, the CLS offers the unique opportunity of estimating the location of the obstacle the. An estimate of the trajectory deviation required to avoid contact can then be formulated using the robot kinematics. In this way, the robot can avoid collision and reduce contact force while not reversing more than necessary. The decreased motion of this method will produce less risk of further collisions with other humans in the surroundings. The possibility of performing a trajectory deviation mediated zero force control with position-controlled robots using the known compliance of the sensor and the measured deformation is currently being pursued.

VII. Conclusion

This paper presented and prototyped the novel CLS for collision detection and reaction during pHRI. The CLS prototype employed five LED/LTV sensor pairs to detect shell motion and estimate external shell pose in the plane using an optimization scheme to resolve the sensor redundancies. Changes in LTV voltages were proposed as a reliable and rapid measure to detect changes in shell pose, and pose estimation was shown capable of following the general motion of the shell while having the potential to run in real time. The application of the CLS to safety in robot–human collisions offers potentially rapid response time with customizable compliance to mitigate injury.

References

[1] A. Pervez and J. Ryu, "Safe physical human robot interaction-past, present and future," *J. Mech. Sci. Technol.*, vol. 22, no. 3, pp. 469–483, 2008.

[2] S. Haddadin, A. Albu-Schäffer, and G. Hirzinger, "Safety evaluation of physical human-robot interaction via crash-testing," in *Proc. Robot., Sci. Syst.*, 2007, vol. 3, pp. 217–224.

[3] S. Haddadin, A. Albu-Schäffer, and G. Hirzinger, "Requirements for safe robots: Measurements, analysis and new insights," *Int. J. Robot. Res.*, vol. 28, nos. 11/12, pp. 1507–1527, 2009.

[4] S. Haddadin, S. Haddadin, A. Khoury, T. Rokahr, S. Parusel, R. Burgkart, A. Bicchi, and A. Albu-Schäffer, "On making robots understand safety: Embedding injury knowledge into control," *Int. J. Robot. Res.*, vol. 31, no. 13, pp. 1578–1602, 2012.

[5] K. Chisholm, K. Klumper, A. Mullins, and M. Ahmadi, "A task oriented haptic gait rehabilitation robot," *Mechatronics*, vol. 24, pp. 1083–1091, Dec. 2014.

[6] B. Povse, D. Koritnik, T. Bajd, and M. Munih, "Correlation between impact-energy density and pain intensity during robot-man collision," in *Proc. IEEE RAS EMBS 3rd Int. Conf. Biomed. Robot. Biomechatron.*, 2010, pp. 179–183.

[7] X. Lamy, F. Colledani, F. Geffard, Y. Measson, and G. Morel, "Robotic skin structure and performances for industrial robot comanipulation," in *Proc. IEEE/ASME Int. Conf. Adv. Intell. Mechatron.*, 2009, pp. 427–432.

[8] S. Haddadin, A. Albu-Schaffer, A. De Luca, and G. Hirzinger, "Collision detection and reaction: A contribution to safe physical human-robot interaction," in *Proc. IEEE/RSJ Int. Conf. Intell. Robots Syst.*, 2008, pp. 3356–3363.

[9] H.-o. Lim and K. Tanie, "Collision-tolerant control of human-friendly robot with viscoelastic trunk," *IEEE/ASME Trans. Mechatron.*, vol. 4, no. 4, pp. 417–427, Dec. 1999.
[10] S.-S. Yoon, S. Kang, S.-k. Yun, S.-J. Kim, Y.-H. Kim, and M. Kim, "Safe arm design with mr-based passive compliant joints and viscoelastic covering for service robot applications," *J. Mech. Sci. Technol.*, vol. 19, no. 10, pp. 1835–1845, 2005.
[11] G. Tonietti, R. Schiavi, and A. Bicchi, "Design and control of a variable stiffness actuator for safe and fast physical human/robot interaction," in *Proc. IEEE Int. Conf. Robot. Autom.*, 2005, pp. 526–531.
[12] M. Zinn, O. Khatib, B. Roth, and J. K. Salisbury, "Playing it safe [human-friendly robots]," *IEEE Robot. Autom. Mag.*, vol. 11, no. 2, pp. 12–21, Jun. 2004.
[13] A. De Santis, B. Siciliano, A. De Luca, and A. Bicchi, "An atlas of physical human–robot interaction," *Mech. Mach. Theory*, vol. 43, no. 3, pp. 253–270, 2008.
[14] A. Stolt, A. Robertsson, and R. Johansson, "Robotic force estimation using dithering to decrease the low velocity friction uncertainties," presented at the IEEE Int. Conf. Robotics Automation, Seattle, WA, USA, May 2015.
[15] M. Linderoth, A. Stolt, A. Robertsson, and R. Johansson, "Robotic force estimation using motor torques and modeling of low velocity friction disturbances," in *Proc. IEEE/RSJ Int. Conf. Intell. Robots Syst.*, 2013, pp. 3550–3556.
[16] J. Ulmen and M. Cutkosky, "A robust, low-cost and low-noise artificial skin for human-friendly robots," in *Proc. IEEE Int. Conf. Robot. Autom.*, 2010, pp. 4836–4841.
[17] R. S. Dahiya, G. Metta, M. Valle, and G. Sandini, "Tactile sensing from humans to humanoids," *IEEE Trans. Robot.*, vol. 26, no. 1, pp. 1–20, Feb. 2010.
[18] O. Kerpa, K. Weiss, and H. Worn, "Development of a flexible tactile sensor system for a humanoid robot," in *Proc. IEEE/RSJ Int. Conf. Intell. Robots Syst.*, 2003, vol. 1, pp. 1–6.
[19] S. Phan, Z. F. Quek, P. Shah, D. Shin, Z. Ahmed, O. Khatib, and M. Cutkosky, "Capacitive skin sensors for robot impact monitoring," in *Proc. IEEE/RSJ Int. Conf. Intell. Robots Syst.*, 2011, pp. 2992–2997.
[20] Y. Yamada, T. Morizono, Y. Umetani, and H. Takahashi, "Highly soft viscoelastic robot skin with a contact object-location-sensing capability," *IEEE Trans. Ind. Electron.*, vol. 52, no. 4, pp. 960–968, Aug. 2005.
[21] M. Frigola, A. Casals, and J. Amat, "Human-robot interaction based on a sensitive bumper skin," in *Proc. IEEE/RSJ Int. Conf. Intell. Robots Syst.*, 2006, pp. 283–287.
[22] M. Inaba, Y. Hoshino, K. Nagasaka, T. Ninomiya, S. Kagami, and H. Inoue, "A full-body tactile sensor suit using electrically conductive fabric and strings," in *Proc. IEEE/RSJ Int. Conf. Intell. Robots Syst.*, 1996, vol. 2, pp. 450–457.
[23] P. Mittendorfer and G. Cheng, "Self-organizing sensory-motor map for low-level touch reactions," in *Proc. IEEE-RAS 11th Int. Conf. Humanoid Robots*, 2011, pp. 59–66.
[24] M. Battaglia, L. Blanchet, A. Kheddar, S. Kajita, and K. Yokoi, "Combining haptic sensing with safe interaction," in *Proc. IEEE/RSJ Int. Conf. Intell. Robots Syst.*, 2009, pp. 231–236.
[25] A. Kadowaki, T. Yoshikai, M. Hayashi, and M. Inaba, "Development of soft sensor exterior embedded with multi-axis deformable tactile sensor system," in *Proc. IEEE 18th Int. Symp. Robot Human Interactive Commun.*, 2009, pp. 1093–1098.
[26] M. Strohmayr, H. Worn, and G. Hirzinger, "The DLR artificial skin step I: Uniting sensitivity and collision tolerance," in *Proc. IEEE Int. Conf. Robot. Autom.*, 2013, pp. 1012–1018.
[27] M. Strohmayr and D. Schneider, "The DLR artificial skin step II: Scalability as a prerequisite for whole-body covers," in *Proc. IEEE/RSJ Int. Conf. Intell. Robots Syst.*, Nov. 2013, pp. 4721–4728.
[28] A. Kulik, J. Hochstrate, A. Kunert, and B. Froehlich, "The influence of input device characteristics on spatial perception in desktop-based 3d applications," in *Proc. IEEE Symp. 3D User Interfaces*, 2009, pp. 59–66.
[29] B. Gombert, "Arrangement for the detection for relative movements or relative position of two objects," U.S. Patent 6 804 012, Oct. 12, 2004.
[30] D. A. Bowman, E. Kruijff, J. J. LaViola Jr, and I. Poupyrev, *3D User Interfaces: Theory and Practice*. Reading, MA, USA: Addison-Wesley, 2004.
[31] S. Zhai, "Human performance in six degree of freedom input control," Ph.D. dissertation, Dept. Ind. Eng., Univ. Toronto, Toronto, ON, Canada, 1995.
[32] (2007). Tsl250r, tsl251r, tsl252r light-to-voltage optical sensors [Online]. TAOS, Inc., Plano, TX, USA. Available: https://www.ams.com
[33] J. J. Moré, "The Levenberg-Marquardt algorithm, implementation and theory," in *Numerical Analysis*. New York, NY, USA: Springer-Verlag, 1978, pp. 105–116.
[34] F. Devernay. (2007). C/c++ minpack [Online]. Available: https://github.com/devernay/cminpack

Colin Miyata received the B.Eng. degree in biomedical and mechanical engineering and the M.A.Sc. degree in biomedical engineering from Carleton University, Ottawa, ON, Canada, in 2013 and 2015, respectively, where he is currently working toward the Ph.D. degree in mechanical engineering at the Advanced Biomechatronics and Locomotion Laboratory.

Kyle Chisholm received the B.Eng. degree in mechanical engineering and the M.A.Sc. degree in rehabilitation robotics from Mechanical Engineering Department, Carleton University, Ottawa, ON, Canada, in 2008 and 2010, respectively, where he is currently working toward the Ph.D. degree at the Advanced Biomechatronics and Locomotion Laboratory.

Jennifer Baba received the B.Sc. degree in mechanical engineering with the biomedical option from the University of New Brunswick, Fredericton, NB, Canada, in 2011. She is currently working toward the Graduate degree at the Advanced Biomechatronics and Locomotion Laboratory, Carleton University, Ottawa, ON, Canada.

From 2009 to 2010, she was a summer Research Assistant with the Institute of Biomedical Engineering studying gait biomechanics and measurement instrument performance. In 2011, she was a Research Assistant studying material identification in mammography with the University of New Brunswick.

Mojtaba Ahmadi (M'04) received the B.Sc. degree from the Sharif University of Technology, Tehran, Iran, in 1989, the M.Sc. degree from the University of Tehran, Tehran, in 1992, and the Ph.D. degree in mechanical engineering from McGill University, Montreal, QC, Canada, in 1998.

He worked on robotic teleoperation and autonomous operation as a Postdoctoral Fellow with the Ecole Polytechnique de Montreal, Montreal, during 1998–2000, and, from 2000 to 2005, he held senior positions in different industries including Opal-RT Technologies, Inc., Montreal, Quantum and Maxtor Corporations, San Jose, CA, USA, and the Institute for Aerospace Research of the National Research Council Canada, Ottawa, ON, Canada. He joined the Department of Mechanical and Aerospace Engineering, Carleton University, Ottawa, in 2005, where he is currently an Associate Professor. He founded the Advanced Biomechatronics and Locomotion Lab and his current research interests include rehabilitation robotics, assistive devices, human–robot interaction, design and control of mechatronics systems, and legged robots.